

See discussions, stats, and author profiles for this publication at: <https://www.researchgate.net/publication/263698912>

Formation of Iron Oxyfluoride Phase on the Surface of Nano-Fe₃O₄ Conversion Compound for Electrochemical Energy Storage

ARTICLE in JOURNAL OF PHYSICAL CHEMISTRY LETTERS · OCTOBER 2013

Impact Factor: 7.46 · DOI: 10.1021/jz402017h

CITATIONS

8

READS

40

10 AUTHORS, INCLUDING:



Jagjit Nanda

Oak Ridge National Laboratory

79 PUBLICATIONS 2,647 CITATIONS

SEE PROFILE



Surendra K Martha

Indian Institute of Technology Hyderabad

63 PUBLICATIONS 1,010 CITATIONS

SEE PROFILE



Sreekanth Pannala

SABIC Americas

107 PUBLICATIONS 849 CITATIONS

SEE PROFILE



Nancy J Dudney

Oak Ridge National Laboratory

191 PUBLICATIONS 5,356 CITATIONS

SEE PROFILE

Formation of Iron Oxyfluoride Phase on the Surface of Nano-Fe₃O₄ Conversion Compound for Electrochemical Energy Storage

Hui Zhou,[†] Jagjit Nanda,^{*,†} Surendra K. Martha,^{†,‡} Jamie Adcock,[‡] Juan C. Idrobo,[†] Loïc Baggetto,[†] Gabriel M. Veith,[†] Sheng Dai,^{‡,§} Sreekanth Pannala,^{||} and Nancy J. Dudney[†]

[†]Materials Science and Technology Division, Oak Ridge National Laboratory, Oak Ridge, Tennessee 37831, United States

[‡]Department of Chemistry, University of Tennessee, Knoxville, Tennessee 37996, United States

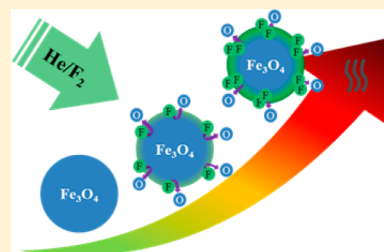
[§]Chemical Science Division, Oak Ridge National Laboratory, Oak Ridge, Tennessee 37831, United States

^{||}Computer Science and Mathematics Division, Oak Ridge National Laboratory, Oak Ridge, Tennessee 37831, United States

Supporting Information

ABSTRACT: We have investigated a novel approach wherein we undertake surface fluorination of nanometer sized Fe₃O₄ conversion compound into corresponding oxyfluoride with the goal toward enhancing their energy density as well electrochemical performance stability. This is achieved by using direct fluorination of nano-Fe₃O₄ in a fluidized bed reactor under controlled reaction atmosphere and temperature. X-ray photoemission spectroscopy analysis shows conclusive evidence of the surface fluorination of Fe₃O₄ particles at a reaction temperature of 100 °C and higher forming a surface oxyfluoride phase that can be nominally described as FeOF. Formation of oxyfluoride phase is confirmed by the appearance of a higher potential intercalation plateau during the electrochemical charge–discharge cycling. Based on the experimental results, various pathways are discussed for the formation of oxyfluoride species on the surface.

SECTION: Energy Conversion and Storage; Energy and Charge Transport



Multivalent conversion-based binary transition metal (TM) compounds have recently gained significant attention due to their higher specific capacity compared to conventional intercalation-based lithium-ion materials.^{1–14} Ideally, this class of materials promise at least 2–3 times higher capacity than single charge carrier based intercalation compounds such as LiFePO₄. It is important to note that while the intercalation-based reactions incur only minor structural changes, the conversion mechanism induce large structural reorganizations during the sequence of multielectron charge transfer steps.¹⁵ As a consequence, it is difficult for multivalent TM materials to exhibit stable reversible capacity over large number of charge–discharge cycles. In addition, the majority of conversion-based compounds such as binary TM fluorides, nitrides, oxides and sulfides are highly electronically insulating. To overcome the electronic insulation in the TM fluorides, nitrides, oxides, and sulfides materials, there have been numerous reports in the literature aimed at facilitating the electron (ion) transport and charge transfer kinetics by materials modifications such as nanosizing, controlling particle shape and morphology, carbon coating and doping.^{16–24}

Iron oxides (Fe₂O₃ and Fe₃O₄) are an important family of conversion compounds with a high specific capacity typically on the order of 1000 mAh/g. The high specific capacity results from the utilization of the multiple oxidation state of Fe:^{5,15,25–28} from Fe³⁺ to Fe⁰. Other advantages of iron oxides materials include low cost, natural abundance, environmental benignity and higher electronic conductivity.^{29–34} Despite such

advantages, iron oxides have a relatively lower redox plateau (below 2 V) with respect to Li/Li⁺, which typically makes them suitable as anodes for lithium battery application. In this study we propose a completely novel approach toward conversion-based oxides such as Iron based. Traditionally for consideration as cathodes, fluorides are consider suitable since they have a relatively higher intercalation (>3 V) as well as conversion redox plateau (2.0 V) compared to their oxide counterparts. However, fluorides are highly ionic compounds and hence are very insulating for application as battery electrodes. To overcome this issue, there has been attempts in the literature to oxidize fluorides to oxyfluorides, thereby making them partly covalent from a purely ionic character.²¹ In this work we aim to follow an alternate route for converting iron oxides to oxyfluorides using a controlled fluorination process. The goal of this study is twofold: (i) controlled fluorination of Fe₃O₄ nanoparticles using a fluidized bed reactor to convert into a oxyfluorides (fluoride) phase and study the evolution of the surface chemistry and structure with reaction parameters and (ii) observe the improvement or increase in the electrochemical capacity and redox potential in the fluorinated phase versus pristine Fe₃O₄. Our results showed that we could only achieve a surface oxyfluoride layer on the Fe₃O₄ when the reaction temperature is >120 °C and at an increased fluorine partial

Received: September 18, 2013

Accepted: October 19, 2013

Published: October 21, 2013

pressure. We notice clear evidence of electrochemical capacity enhancement with a concomitant increase in voltage plateau on fluorination as demonstrated in the electrochemical cycling, differential capacity, and cyclic voltammetry results.

Fe_3O_4 , generally known as magnetite, has an inverse spinel structure, which can be written as $\text{Fe}^{3+}[\text{Fe}^{2+}\text{Fe}^{3+}]\text{O}_4$, where the O^{2-} ions are cubic close packed to build the framework; half of Fe^{3+} ions occupy the octahedral sites together with the Fe^{2+} ions and the other half Fe^{3+} ions occupy the tetrahedral sites (Figure S1, Supporting Information).³⁵ We performed high-resolution STEM studies in conjunction with EELS to study the structure of pristine as well as fluorinated $\text{n-Fe}_3\text{O}_4$. The atomic-scale images of several individual particles of pristine Fe_3O_4 are shown in Figure 1a. The primary Fe_3O_4 particle size

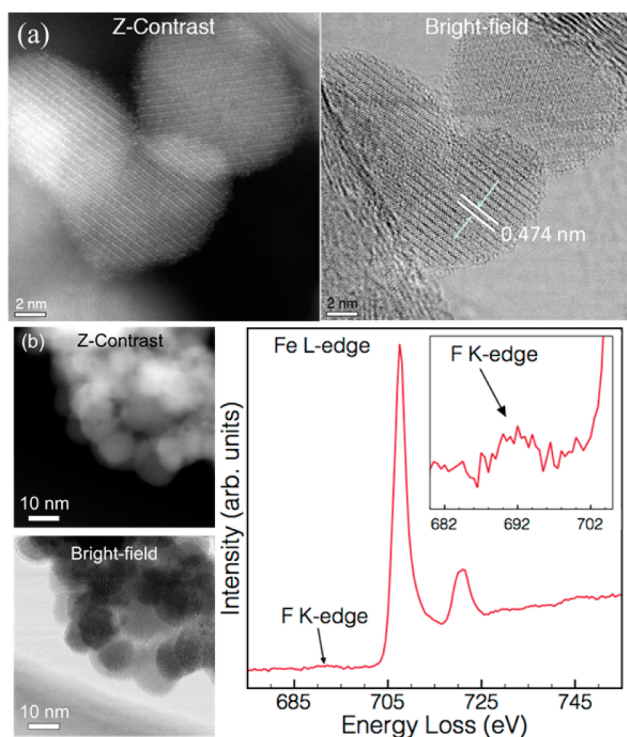


Figure 1. (a) Local structural analysis of the pristine Fe_3O_4 particles: Z-contrast and bright-field STEM images. The lattice resolved images are obtained with electron beam parallel to the $[211]$ and $[013]$ zone axis. (b) Magnified STEM images of one agglomerated secondary particle of the fluorinated sample and corresponding EEL spectra for Fe L- and F K-edges.

is about 10 nm and the Z-contrast as well as bright field image showing that the interplanar distance of the nanoparticles are 0.474 nm (Figure 1a), which can be assigned to the (111) planes respectively. Interestingly, according to a recent published report by Zeng et al.,³⁶ the (111) plane of Fe_3O_4 has lower electrochemical activity compared to other planes, a factor that can account for the poor electrochemical property of this material. The morphology and particle size of $\text{n-Fe}_3\text{O}_4$ looks similar for the samples before and after the fluorination, except that the pristine particles appear more agglomerated after the fluorination (Figure S3). EELS experiments for elemental analysis were carried for the 120 and 150 °C fluorinated $\text{n-Fe}_3\text{O}_4$ samples. The results are shown in Figure 1b: apart from a strong Fe peak, a very weak F signal can also be observed, which indicates the presence of fluorinated species on the sample after the fluorination process. The EELS spectra

were obtained while scanning the electron probe across the whole area shown in Figure 1b in order to improve the signal-to-noise ratio for the F K-edge. The weak F K-edge signal is due to a number of factors, (i) fluorine gets removed during the large dwell times required for the EELS experiments (~ 0.5 s/pixel) and (ii) the samples only have shallow fluorination on the surface. A magnified version of the F K edge is shown in the inset of Figure 1b. The results are further corroborated by our X-ray diffraction (XRD) and X-ray photoelectron spectroscopy (XPS) studies.

XRD studies were performed on the fluorinated $\text{n-Fe}_3\text{O}_4$ samples to study the changes in the structure as a result of fluorination. As shown in Figure 2. The patterns look similar for the pristine as well as for the fluorinated samples implying there are no major structural or phase changes. A careful comparison (see Supporting Information) of the two main XRD peaks at low and high angles (insets of Figure 2a), shows a systematic peak shift toward higher 2θ with increasing fluorination temperature beyond 100 °C. The positions of (311) and (440) XRD peaks at different fluorination temperatures is shown in Figure 2b. Detailed lattice parameter decrease and unit cell volume changes based on Rietveld refinement method is presented in the Supporting Information (Figure S5).

As discussed earlier, Fe_3O_4 is a mixed valent phase of iron oxide, which can be written as $\text{Fe}_2\text{O}_3 \cdot \text{FeO}$. It is possible that some of the FeO on the surface may be oxidized by fluorination, causing more Fe^{3+} present in the sample with increased fluorination. This could result in a slight reduction of lattice parameters, since Fe^{3+} has a smaller ionic radius than Fe^{2+} (0.645 Å vs 0.78 Å). In addition, substitution of O^{2-} (1.4 Å) by the slightly smaller F^- (1.33 Å) on the surface may also contribute to the reduction of the lattice parameter. The slight peak shift, combined with the very weak F signal obtained by EELS, indicates that the fluorination mainly happens on the surface of the material. To further evaluate the surface chemistry before and after fluorination, XPS was performed.

Elemental ratio was analyzed at first to see the change of F content in the sample. Figure 3a shows the change of atomic ratio of O/Fe and F/Fe with the increased fluorination temperatures which were calculated by the area ratio of the respective XPS core level signal of O 1s, F 1s, and Fe 2p peaks. The results show that as the temperature increases, more F is introduced into the sample with concomitant reduction of surface oxygen species. The F/Fe ratio suggests that the fluorination reactions are more activated at temperatures >100 °C. This observation is consistent with our XRD results that shows peak shift for the samples fluorinated above 100 °C.

To be consistent, we also analyzed other Fe core levels such as Fe 3s and Fe 3p. The typical Fe 3s photoelectron spectra of the samples before and after the fluorination are compared in Figure 3b. From the figure, it is clearly seen that with increased fluorination, the peaks gradually shift toward the higher binding energy (as shown by the arrows); this is consistent with F being more electronegative compared to O, which will shift Fe 3s spectrum to higher B.E.³⁷ (except for the 25 °C sample). The spectral deconvolution and the results are summarized in Table 1. The Fe 3s has a doublet structure, which has its origin due to the exchange coupling between the 3s vacancy and the 3d electrons.³⁸ The value of the splitting is sensitive to the number of unpaired 3d-electron of the metal atom, so it can provide information about the formal oxidation state of the transition metal.^{38,39} Generally this splitting is about 6.2 eV for Fe^{3+} and about 5.5 eV for Fe^{2+} in simple iron oxides.^{40,41} For our

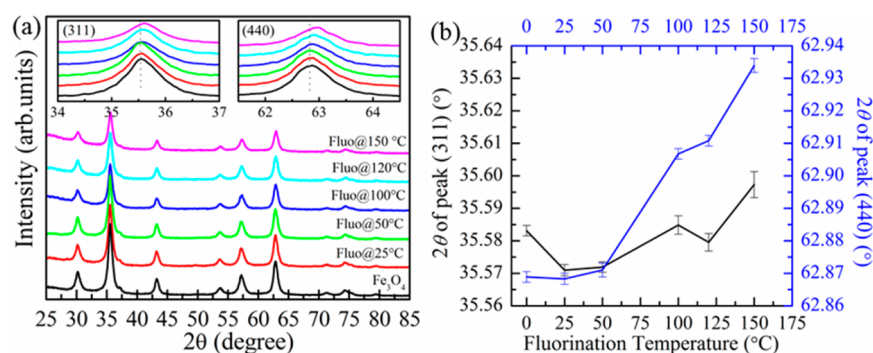


Figure 2. (a) Comparison of XRD patterns for the Fe₃O₄ samples before and after the fluorinations. The inset two figures show the expanded view of two main XRD peaks: (311) and (440). The dashed line indicates the original peak positions of the pristine Fe₃O₄. (b) The change of the positions of peaks (311) and (440) with the fluorination temperatures. The positions of these two peaks for starting material are almost same as the 25 °C sample.

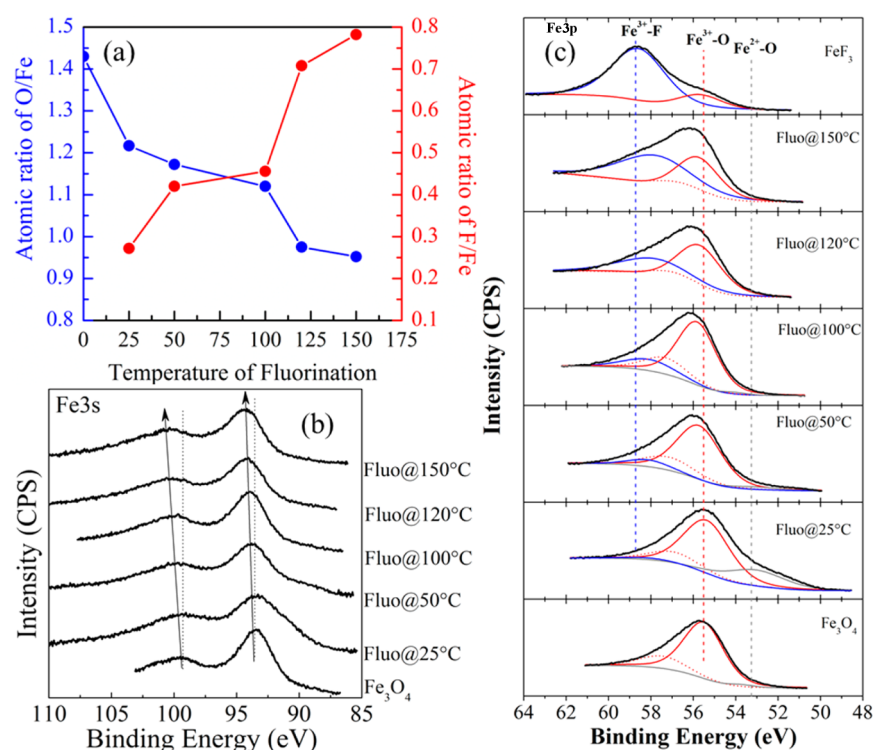


Figure 3. (a) Change of the ratio of O/Fe and F/Fe with increased fluorination temperatures, which were calculated on the XPS data of O 1s, F 1s, and Fe 2p peaks. (b) Fe 3s photoelectron spectra of the Fe₃O₄ samples before and after the fluorination. The dashed lines indicate the original position of the pristine Fe₃O₄. The Arrows show the shifting trend of the peaks positions with fluorinations. (c) Fe 3p photoelectron spectra of the Fe₃O₄ samples before and after the fluorinations. The deconvoluted peaks are also shown. The solid blue, red, and gray lines are the positions of the Fe³⁺-F, Fe³⁺-O, and Fe²⁺-O bonds respectively, using FeF₃ and Fe₃O₄ as the references.

Table 1. The Results for Fe 3s Photoelectron Spectra Deconvolution^a

sample	Fe 3s		
	peak 1	peak 2	splitting
Fe ₃ O ₄	93.24	99.24	6.0
Fluo@25 °C	93.29	99.24	5.95
Fluo@50 °C	93.71	99.76	6.05
Fluo@100 °C	93.92	100.01	6.09
Fluo@120 °C	94.25	100.37	6.12
Fluo@150 °C	94.33	100.51	6.18

^aBinding energy in eV.

samples, the splitting of the starting material is about 6.0 eV, which is in good agreement with the mixed valent nature of Fe in Fe₃O₄. With increased fluorination temperature, the value of splitting increases gradually, indicating more and more Fe³⁺ in the sample, possibly forming phases of iron oxyfluoride. We expect such phase to be formed mostly on the surface of Fe₃O₄ particles since the XRD does not show any indication of new oxyfluoride phase.

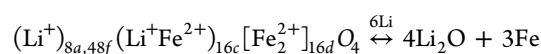
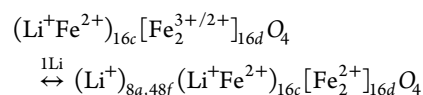
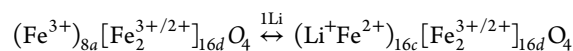
The corresponding Fe 3p XPS core level analysis as a function of fluorination temperatures are shown in Figure 3c. The spectral analysis is complicated due to the multiplet structure originating from the Fe 3p–3d exchange interaction^{39,42} and the intrinsic spin–orbit coupling (3p_{3/2} and 3p_{1/2}). Since the spin–orbit coupling energy is much smaller

we do not factor this in the spectral fitting and account only for the multiplet effect. To observe the chemical shift upon fluorination we also show the Fe 3p core level of FeF₃ and the pristine Fe₃O₄. For Fe₃O₄ we primarily see three main chemical surroundings: Fe³⁺–O feature around 55.6 eV (red solid line) consistent with previous report,⁴³ multiplet peak around 57.5 eV (red dash line), and a weak feature around 53.4 eV (gray solid line) from the Fe²⁺–O. Since Fe₃O₄ can be described as Fe₂O₃·FeO, it shows from XPS that the surface is mostly Fe₂O₃. The end member FeF₃ understandably has the dominant Fe³⁺–F peak at 58.4 eV (blue solid line) but also has an oxidized species Fe³⁺–O. With surface fluorination we see two major peak shifts which gradually increase with temperature. The Fe³⁺–O feature moves toward higher BE (red solid line) and concomitantly there appears to be another high BE component that is more typical to the Fe³⁺–F environment. The BE shift completely follows the trend with higher electronegative F atom substituting O around Fe. Such spectral evolution as a function of increasing fluorination temperatures indicates that we have formation of FeOF type composition on the surface where the Fe is coordinated with both oxygen and fluorine atoms. F 1s photoelectron spectra gave the similar results as well (Figure S6). For the fluorinated samples at low temperatures (below 100 °C), besides the main F 1s peak around 685 eV, there is another small feature located at higher binding energy side whose origin is not known yet. This could be small amount of F adsorbed on the surface. At higher temperature, we notice only one symmetric peak, indicating the existence of a single F phase at higher fluorination.

Based on the XPS analysis, we can hypothesize that the fluorination process proceeds through the following steps: (i) initially at 25 °C fluorination, F atoms get adsorbed on the surface of the Fe₃O₄ particles eventually displacing the O atoms and/or occupy vacant O sites to have a nominal stoichiometry of Fe₃O_{4–x}F_x. This corroborates with reduction of O/Fe and the increase of F/Fe ratio at 25 °C (Figure 3a) and slight decrease in the exchange splitting value of Fe 3s XPS peak (5.95 versus 6.0 eV, Table 1), (ii) with further increase in temperature, more F will take part in the reaction with potentially two F atoms substituting one O with a oxyfluoride composition that can be described as Fe₃O_{4–x}F_{2x}. This coincides with a sharp increase of F/Fe ratio between 25 and 50 °C (Figure 3a). However, such substitutions may mainly occur at the oxygen sites that coordinate with Fe³⁺ of the Fe₃O₄ mixed valent lattice, because there may not be sufficient activation energy to oxidize the Fe²⁺ sites to Fe³⁺, (iii) increasing the reaction temperature as well as F gas concentration could lead to the oxidation of Fe²⁺ sites and subsequent formation of the oxyfluoride phase as shown by another sharp increase of F/Fe ratio. The final surface composition for the 150 °C fluorinated sample calculated from the elemental ratio (Figure 3a) is FeO_{0.952}F_{0.782}. We also find a small amount of carbon on the sample surface corresponding to C–O and O–C=O functionality. The C1s spectrum is shown in the Supporting Information, Figure S7. Based on the O and C XPS signal in the fluorinated Fe₃O₄ samples, we found at least 10% of the O is contributed from the bonds with C. Correcting for this factor, the final composition is very close to FeOF, indicating that the surface is almost completely converted to oxyfluoride. The surface oxyfluoride could be either amorphous or too thin to be observed in XRD as a separate phase. Nevertheless, this surface oxyfluoride phase

has an important implication toward the electrochemical performance as described in the next section.

To observe the effect of the fluorination on the electrochemical properties of the samples, three fluorinated samples above 100 °C were chosen for the electrochemical tests and compared to the performance of the starting material nano-Fe₃O₄ powder. The electrochemical reaction between Fe₃O₄ and Li can be expressed as Fe₃O₄ + 8Li ↔ 4Li₂O + 3Fe, a total of eight electrons are involved in the reaction and yields a theoretical capacity of around 924 mAh/g. The entire reaction step can be divided into three parts:⁴⁴



the first two parts are the intercalation reactions, where Fe was reduced from Fe³⁺ to Fe²⁺: initially the 8a-Fe³⁺ ions are cooperatively displaced to octahedral sites 16c with first Li insertion, and the further lithiation (second part) involves a filling of the tetrahedral sites by the inserted Li⁺ ions; the third part is the conversion reaction, where the Fe was replaced by Li and produce Li₂O and Fe. The thermodynamic values reported for conversion reaction for Iron oxides is about 0.8 V and the intercalation reaction plateau is above 1.0 V.⁴⁵

Figures 4 and 5 summarize the electrochemical performance of fluorinated n-Fe₃O₄ compounds compared to pristine Fe₃O₄. The effect of fluorination on the voltage plateau and peaks can be shown more clearly in the cyclic voltammetry (CV) and differential capacity plots shown in Figure 4a–c. Broadly, we notice a peak around 1.6 V due to first intercalation reaction as discussed earlier. This peak understandably shifts to higher voltage upon fluorination. Another sharp peak at around 1 V shown in the CV plot is possibly the contribution from second intercalation reaction. The information obtained from CV here is purely qualitative and could also depend on the scan rate, stability of reference electrodes and other parameters. To gain further insights on the effect of fluorination, we performed a dQ/dV analysis of the first cycling profile. As shown in Figure 4b, for the pristine Fe₃O₄ sample (gray plot), there are two reduction peaks in the >1.0 V region, around 1.7 and 1.2 V respectively, which should correspond to the two intercalation reactions as we discussed in context of our CV results. Interestingly, another reduction peak around 0.8–0.7 V appears if one extends the voltage range to lower cutoff voltage below 1 V, this is related to the conversion process as reported earlier (not shown here).^{15,24} At fluorination till 100 °C, no major changes (black solid line Figure 4b,c) can be observed, except we notice a shift of the intercalation peaks to the higher potential, plausibly caused by the substitution of O by F on the surface and the increased ionicity of Fe–F compared to Fe–O. For the samples fluorinated at even higher temperatures (120 and 150 °C), the peaks are further shifted (red and blue solid lines) to approximately 1.8 V. In addition we also notice a broad reduction feature at 3.0 V with a similar oxidation counterpart closely resembling the reported results for FeOF.²¹ We also observe a small reduction peaks at around 1.4 V, in the fluorinated samples whose origin is yet to be understood. Thus

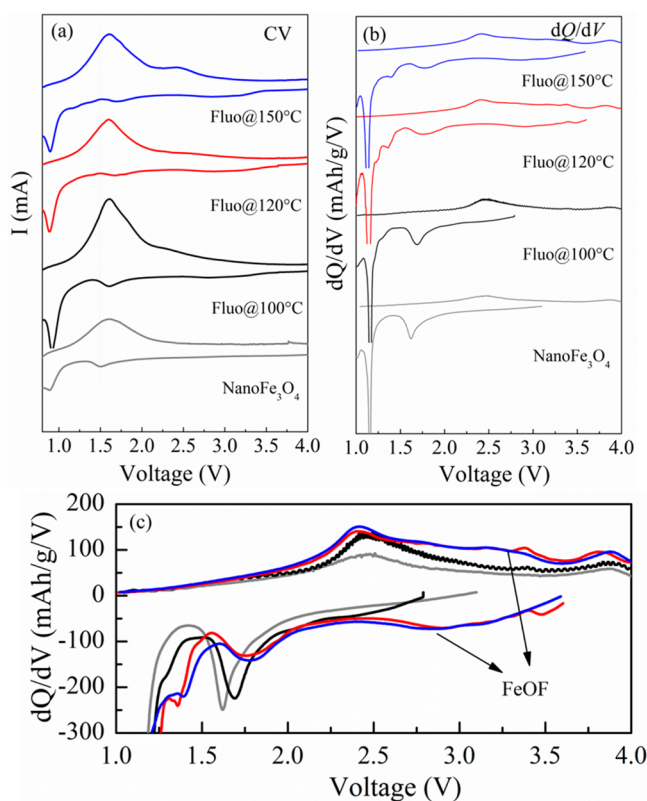


Figure 4. (a) The cyclic voltammetry of the first cycle for the Fe₃O₄ powder and that fluorinated at 100, 120, and 150 °C in the voltage range of 4.5–0.5 V with the scanning rate of 0.05 mV/s. (b) dQ/dV of the first cycling profile. (c) dQ/dV curves showing redox peaks above 1.5 V.

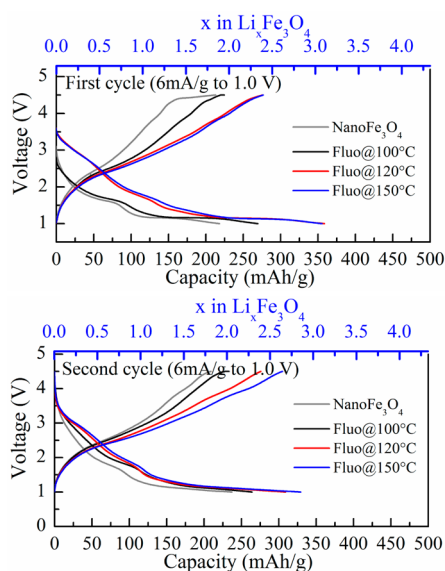


Figure 5. The cycling curves of the first two cycles for the Fe₃O₄ powder and that fluorinated at 100, 120, and 150 °C in the voltage range of 4.5–1.0 V with the current density of 6 mA/g. The amount of Li involved in the electrochemical reactions is also shown.

the electrochemical performance of the fluorinated samples has mixed signatures characteristic of Fe₃O₄ and FeOF.

The capacity contribution from conversion reaction falls in a voltage region where there is a possibility of contribution from

other sources such as electrolyte reduction or lithiation of current collector etc., so for our electrochemical performance comparison between pristine and fluorinated electrodes, we limit the voltage window to 4.5–1.0 V. Traditionally, for iron oxides the upper cutoff voltage is usually 3 or 3.5 V,²⁴ but in our case it is 4.5 V since we notice capacity contribution at higher voltage upon fluorination. We notice significant improvement in the capacity of fluorinated samples compared to pristine Fe₃O₄ in the intercalation window as shown for first two cycles in Figure 5 (upper and lower panel). The capacity gradually increases from 240 mAh/g for pristine to about 340 mAh/g for 150 °C fluorination. Especially for the two fluorinated samples at 120 and 150 °C, we notice reversible >2 intercalated Li when cycled till 1 V cutoff. It is plausible that such an increase in capacity from fluorinated samples could be due to more Fe³⁺ state on the surface due to the formation of oxyfluoride phase compared to the pristine Fe₃O₄ as discussed in the context of XPS analysis.

It is noteworthy to mention that in our study the starting nano-Fe₃O₄ material was not optimized for electrochemical performance but rather to demonstrate the concept of oxyfluoride conversion. The experimental result provides a proof of principle electrochemical signature that even a small surface layer of oxyfluoride formation on Fe₃O₄ can have noticeable impact. It is plausible to get even better electrochemical performance if we could start with nanophases of Fe₃O₄ that are optimized for electrochemistry as shown in a few literature studies.

In this work we have investigated the surface chemistry, structure and electrochemical response of a conversion electrode material, Fe₃O₄ on fluorination. The fluorination process was carried out by using temperature controlled fluidized bed reactor setup where nanoparticles of Fe₃O₄ was exposed to F₂ gas in a controlled atmosphere. XPS analysis showed evidence of surface oxide phase converting to oxyfluoride with increase fluorination temperature. There was no substantial change in the structure of n-Fe₃O₄ upon fluorination as observed from XRD analysis. We only notice a slight reduction of the lattice parameter due to F substitution. We also observe interesting electrochemical response of fluorinated Fe₃O₄ compared to pristine. Signature of improved electrochemical performance upon fluorination is the increase in the intercalation voltage plateau. The intercalation discharge plateau appears to be more like FeOF rather than Fe₃O₄.²¹ This rise of the intercalation potential could be clearly an effect of the formation of surface oxyfluoride phase due to increased ionicity of Fe–F bonds compared to Fe–O. Additionally we also notice an increase in the intercalation capacity in the case of fluorinated samples compared to pristine n-Fe₃O₄.

EXPERIMENTAL METHODS

All the fluorinations are conducted in a fluidized bed fluorination reactor (FBR). The reactor is connected to a mixing device consisting of a Hastings flow transducer calibrated for fluorine and a rotameter gauge flowmeter for helium gas. The apparatus allows He/F₂ mixtures from 0 to 100% F₂ to flow into the FBR tube. Before fluorination, the nano Fe₃O₄ powders (Inframmat Advanced Materials LLC, CT, USA) are dried at 150 °C under vacuum (<10 mTorr) overnight. Then the dehydrated sample powder is placed in an FBR tube and sealed by Teflon tape on the sealing surfaces. The FBR tube is purged for 90 min with 46 sccm (for fluorination at 25 °C, 50 and 100 °C) or 23 sccm (for

fluorination at 120 and 150 °C) He, while the temperature of the FBR tube is ramped to the set temperature. After 30 min, the fluorine gas at 2.2 sccm (for fluorination at 25 °C, 50 and 100 °C) or 2.4 sccm (for fluorination at 120 and 150 °C) is introduced into the reactor along with the He flow. After the allotted reaction time, the heat is shut off along with the fluorine flow, and FBR is allowed to cool and be slowly purged with He. The FBR is detached, sealed, and carried into a N₂ filled drybox where the fluorinated sample is transferred to a fluorinated vial and weighed. The FBR method used in this study for conversion of iron oxide to oxyfluorides using low pressure fluorine gas mixed with an inert carrier gas (He) is a relatively simple and safe process used routinely for fluorination studies.⁴⁶

The structure of the samples is characterized by X-ray powder diffraction (XRD) through a Scintag PDS 2000 diffractometer equipped with Cu K α source and Ni filter (λ = 1.54178 Å). Data are collected over the range of 5–90° 2 θ with a step size of 0.02° and dwell time of 1 s; longer dwell time (5 s) is used for the refinement of the XRD data. The Rietveld refinement of the XRD patterns is done using the GSAS/EXPGUI package.⁴⁷ Scanning transmission electron microscopy (STEM) imaging and electron energy-loss spectroscopy (EELS) were performed in an aberration-corrected dedicated scanning transmission electron microscope, Nion UltraSTEM 100, which has a cold field-emission electron source and that can correct third and fifth-order aberrations.⁴⁸ The microscope was operated at 100 kV acceleration voltage. A 30 mrad convergence angle, a 48 mrad collection aperture, an energy dispersion of 0.5 eV/pixel, and an electron beam with an energy resolution of 350 meV were used in the electron energy loss spectroscopy (EELS) experiments.

Surface chemistry and composition analysis is measured using a PHI 3056 X-ray photoelectron spectroscopy (XPS) spectrometer with an Al source in a 2×10^{-8} Torr vacuum chamber. High-resolution scans are taken with 23.5 eV pass energy, 0.05 eV energy step, and 80–100 repeats to improve the signal-to-noise ratio. Survey scans are measured at 93.9 eV pass energy, 0.25 eV energy step, and 10 repeats. The C 1s XPS core level spectrum at a BE value of 284.8 eV arising from the adventitious carbon present on the sample (or XPS chamber) was used as reference for correcting of sample charging. The atomic concentrations on the surface are calculated by integrating the peaks' area and using the standard atomic sensitivity factors supplied by the equipment manufacturer. The spectra are deconvoluted through Gaussian–Lorentzian functions and a Shirley-type background.

The electrochemical properties of these samples are evaluated in two-electrode coin-type cells (size 2032, Hohsen Corp. Japan) on a Maccor multichannel battery tester (model 4000, Maccor Inc., Tulsa, OK, USA) using pure lithium foil (purity 99.9%, Alfa Aesar) as the counter electrode. The cathode is prepared by mixing each sample with multilayer graphene (MLG) and poly(vinylidene fluoride) (PVDF) powder in a weight ratio of 50:40:10 in NMP (*N*-methylpyrrolidone) with a Turbula Shaker-Mixer (Glen Mills Inc., NJ, USA). After mixing for about 30 min, the homogeneous paste is cast on the Al foil and then dried in vacuum oven at 90 °C for overnight. The typical loading of the electrode is around 2 mg/cm² with the electrode area of 1.0 cm². The electrode composition in our case has 40% graphitic platelets or MLG as electronic diluent. Since Fe₃O₄ is not electronically insulating; the electrode also works well even at

lower carbon composition such as 80:10:10 (Fe₃O₄:MLG:PVDF). We have verified this experimentally (data not shown here). The electrolyte is 1.2 M LiPF₆ (lithium hexafluorophosphate) dissolved in a mixture solution of EC (ethylene carbonate) and dimethyl carbonate (DMC) (battery grade, Novolyte Technologies, USA) in a volume ratio of 3:7 with HF and H₂O impurity less than 50 and 5 ppm respectively; Celgard 2325 separator (Celgard Inc., USA) is used. The assembling of the coin cells are done in high purity argon filled glovebox. The charge–discharge cycling (at 25 °C) is performed between 1.0–4.5 V with current density of 6 mA/g and 20 mA/g respectively. Cyclic voltammetry is performed using a VMP multichannel VSP potentiostat (Bio-Logic) by two electrode coin cells with pure lithium foil as both reference and counter electrode, which is scanned between 0.5–4.5 V with the rate of 0.05 mV/s.

■ ASSOCIATED CONTENT

● Supporting Information

Structure of Fe₃O₄; local structural analysis of Fe₃O₄ particles; STEM images of the pristine Fe₃O₄ and the fluorinated sample at 120 °C; F 1s and C 1s photoelectron spectra of the pristine Fe₃O₄ and the fluorinated samples at different temperatures; determination of the XRD shift after fluorination with the standard XRD reference-Mica; evolution of the lattice parameters as a function of the fluorination temperatures based on the Rietveld refinement. This material is available free of charge via the Internet at <http://pubs.acs.org>.

■ AUTHOR INFORMATION

Corresponding Author

*E-mail: nandaj@ornl.gov.

Present Address

[†]Department of Chemistry, Indian Institute of Technology Hyderabad, Ordnance Factory Estate, Yeddumailaram 502 205, A.P., India.

Notes

The authors declare no competing financial interest.

■ ACKNOWLEDGMENTS

This research is supported by the Laboratory Directed Research and Development Program of Oak Ridge National Laboratory, managed by UT-Battelle, LLC, for the U.S. Department of Energy (H.Z., J.N., S.K.M., J.C.I., S.D., S.P.). Electron microscopy work is supported by Oak Ridge National Laboratory's Shared Research Equipment (ShaRE) User Facility Program, which is funded by Office of Basic Energy Sciences, DOE (JCI). Research partially supported by the U.S. Department of Energy, Basic Energy Sciences, Materials Sciences and Engineering Division (G.M.V., L.B. - XPS).

■ REFERENCES

- (1) Wagner, F. T.; Lakshmanan, B.; Mathias, M. F. Electrochemistry and the Future of the Automobile. *J. Phys. Chem. Lett.* **2010**, *1*, 2204–2219.
- (2) Makimura, Y.; Rougier, A.; Laffont, L.; Womes, M.; Jumas, J. C.; Leriche, J. B.; Tarascon, J. M. Electrochemical Behaviour of Low Temperature Grown Iron Fluoride Thin Films. *Electrochem. Commun.* **2006**, *8*, 1769–1774.
- (3) Plitz, I.; Badway, F.; Al-Sharab, J.; DuPasquier, A.; Cosandey, F.; Amatucci, G. G. Structure and Electrochemistry of Carbon–Metal Fluoride Nanocomposites Fabricated by Solid-State Redox Conversion Reaction. *J. Electrochem. Soc.* **2005**, *152*, A307.

- (4) Oumellal, Y.; Rougier, A.; Nazri, G. A.; Tarascon, J. M.; Aymard, L. Metal Hydrides for Lithium-Ion Batteries. *Nat. Mater.* **2008**, *7* (11), 916–21.
- (5) Li, H.; Balaya, P.; Maier, J. Li-Storage via Heterogeneous Reaction in Selected Binary Metal Fluorides and Oxides. *J. Electrochem. Soc.* **2004**, *151*, A1878.
- (6) Xiong, H.; Slater, M. D.; Balasubramanian, M.; Johnson, C. S.; Rajh, T. Amorphous TiO₂ Nanotube Anode for Rechargeable Sodium Ion Batteries. *J. Phys. Chem. Lett.* **2011**, *2*, 2560–2565.
- (7) Prakash, R.; Mishra, A. K.; Roth, A.; Kübel, C.; Scherer, T.; Ghafari, M.; Hahn, H.; Fichtner, M. A Ferrocene-Based Carbon–Iron Lithium Fluoride Nanocomposite as A Stable Electrode Material in Lithium Batteries. *J. Mater. Chem.* **2010**, *20*, 1871.
- (8) Wang, F.; Robert, R.; Chernova, N. A.; Pereira, N.; Omenya, F.; Badway, F.; Hua, X.; Ruotolo, M.; Zhang, R.; Wu, L.; et al. Conversion Reaction Mechanisms in Lithium Ion Batteries: Study of the Binary Metal Fluoride Electrodes. *J. Am. Chem. Soc.* **2011**, *133*, 18828–36.
- (9) Yamakawa, N.; Jiang, M.; Key, B.; Grey, C. P. Identifying the Local Structures Formed during Lithiation of the Conversion Material, Iron Fluoride, in a Li Ion Battery: A Solid-State NMR, X-ray Diffraction, and Pair Distribution Function Analysis Study. *J. Am. Chem. Soc.* **2009**, *131*, 10525–10536.
- (10) Yin, W.-J.; Wei, S.-H.; Ban, C.; Wu, Z.; Al-Jassim, M. M.; Yan, Y. Origin of Bonding between the SWCNT and the Fe₃O₄(001) Surface and the Enhanced Electrical Conductivity. *J. Phys. Chem. Lett.* **2011**, *2*, 2853–2858.
- (11) Zhang, N.; Yi, R.; Wang, Z.; Shi, R.; Wang, H.; Qiu, G.; Liu, X. Hydrothermal Synthesis and Electrochemical Properties of Alpha-Manganese Sulfide Submicrocrystals as an Attractive Electrode Material for Lithium-ion Batteries. *Mater. Chem. Phys.* **2008**, *111*, 13–16.
- (12) Poizot, P.; Laruelle, S.; Grugeon, S.; Dupont, L.; Tarascon, J. M. Nano-Sized Transition-Metaloxides as Negative-Electrode Materials for Lithium-Ion Batteries. *Nature* **2000**, *407*, 496–499.
- (13) Yamakawa, N.; Jiang, M.; Grey, C. P. Investigation of the Conversion Reaction Mechanisms for Binary Copper(II) Compounds by Solid-State NMR Spectroscopy and X-ray Diffraction. *Chem. Mater.* **2009**, *21*, 3162–3176.
- (14) Manthiram, A. Materials Challenges and Opportunities of Lithium Ion Batteries. *J. Phys. Chem. Lett.* **2011**, *2*, 176–184.
- (15) Cabana, J.; Monconduit, L.; Larcher, D.; Palacin, M. R. Beyond Intercalation-based Li-ion Batteries: The State of the Art and Challenges of Electrode Materials Reacting through Conversion Reactions. *Adv. Mater.* **2010**, *22*, E170–92.
- (16) Kim, S. W.; Seo, D. H.; Gwon, H.; Kim, J.; Kang, K. Fabrication of FeF₃ Nanoflowers on CNT Branches and Their Application to High Power Lithium Rechargeable Batteries. *Adv. Mater.* **2010**, *22*, S260–S264.
- (17) Liu, L.; Zhou, M.; Yi, L.; Guo, H.; Tan, J.; Shu, H.; Yang, X.; Yang, Z.; Wang, X. Excellent Cycle Performance of Co-Doped FeF₃/C Nanocomposite Cathode Material for Lithium-Ion Batteries. *J. Mater. Chem.* **2012**, *22*, 17539.
- (18) Muraliganth, T.; Vadivel Murugan, A.; Manthiram, A. Facile Synthesis of Carbon-Decorated Single-Crystalline Fe₃O₄ Nanowires and Their Application as High Performance Anode in Lithium Ion Batteries. *Chem. Commun. (Cambridge, U. K.)* **2009**, *47*, 7360–2.
- (19) Jeong, G. H.; Bae, H.-B.; Choi, D.; Kim, Y. H.; Yoon, S.; Kim, S.-W. Highly Stable Metal Mono-Oxide Alloy Nanoparticles and Their Potential as Anode Materials for Li-Ion Battery. *J. Phys. Chem. C* **2012**, *116*, 23851–23857.
- (20) Ji, L.; Toprakci, O.; Alcoutlabi, M.; Yao, Y.; Li, Y.; Zhang, S.; Guo, B.; Lin, Z.; Zhang, X. Alpha-Fe₂O₃ Nanoparticle-Loaded Carbon Nanofibers as Stable and High-Capacity Anodes for Rechargeable Lithium-Ion Batteries. *ACS Appl. Mater. Interfaces* **2012**, *4*, 2672–9.
- (21) Pereira, N.; Badway, F.; Wartelsky, M.; Gunn, S.; Amatucci, G. G. Iron Oxyfluorides as High Capacity Cathode Materials for Lithium Batteries. *J. Electrochem. Soc.* **2009**, *156*, A407.
- (22) Xu, X.; Cao, R.; Jeong, S.; Cho, J. Spindle-like Mesoporous Alpha-Fe₂O₃ Anode Material Prepared from MOF Template for High-Rate Lithium Batteries. *Nano Lett.* **2012**, *12*, 4988–91.
- (23) Li, J.; Dahn, H. M.; Krause, L. J.; Le, D.-B.; Dahn, J. R. Impact of Binder Choice on the Performance of α -Fe₂O₃ as a Negative Electrode. *J. Electrochem. Soc.* **2008**, *155*, A812–A816.
- (24) Zhou, G.; Wang, D.-W.; Li, F.; Zhang, L.; Li, N.; Wu, Z.-S.; Wen, L.; Lu, G. Q.; Cheng, H.-M. Graphene-Wrapped Fe₃O₄ Anode Material with Improved Reversible Capacity and Cyclic Stability for Lithium Ion Batteries. *Chem. Mater.* **2010**, *22*, 5306–5313.
- (25) Chen, J.; Xu, L. N.; Li, W. Y.; Gou, X. L. Alpha-Fe₂O₃ Nanotubes in Gas Sensor and Lithium-Ion Battery Applications. *Adv. Mater.* **2005**, *17*, 582.
- (26) Thackeray, M. M.; Coetzer, J. A. Preliminary Investigation of the Electrochemical Performance of Alpha-Fe₂O₃ and Fe₃O₄ Cathodes in High-Temperature Cells. *Mater. Res. Bull.* **1981**, *16*, 591–597.
- (27) Muruganandham, M.; Amutha, R.; Sathish, M.; Singh, T. S.; Suri, R. P. S.; Sillanpää, M. Facile Fabrication of Hierarchical α -Fe₂O₃: Self-Assembly and Its Magnetic and Electrochemical Properties. *J. Phys. Chem. C* **2011**, *115*, 18164–18173.
- (28) Zhang, L.; Wu, H. B.; Madhavi, S.; Hng, H. H.; Lou, X. W. Formation of Fe₂O₃ Microboxes with Hierarchical Shell Structures from Metal–Organic Frameworks and Their Lithium Storage Properties. *J. Am. Chem. Soc.* **2012**, *134*, 17388–91.
- (29) Mitra, S.; Poizot, P.; Finke, A.; Tarascon, J. M. Growth and Electrochemical Characterization versus Lithium of Fe₃O₄ Electrodes Made by Electrodeposition. *Adv. Funct. Mater.* **2006**, *16*, 2281–2287.
- (30) Ban, C.; Wu, Z.; Gillaspie, D. T.; Chen, L.; Yan, Y.; Blackburn, J. L.; Dillon, A. C. Nanostructured Fe₃O₄/SWNT Electrode: Binder-Free and High-Rate Li-Ion Anode. *Adv. Mater.* **2010**, *22*, E145–E149.
- (31) Zhang, W.-M.; Wu, X.-L.; Hu, J.-S.; Guo, Y.-G.; Wan, L.-J. Carbon Coated Fe₃O₄ Nanospindles as a Superior Anode Material for Lithium-Ion Batteries. *Adv. Funct. Mater.* **2008**, *18*, 3941–3946.
- (32) Lin, Y.-M.; Abel, P. R.; Heller, A.; Mullins, C. B. α -Fe₂O₃ Nanorods as Anode Material for Lithium Ion Batteries. *J. Phys. Chem. Lett.* **2011**, *2*, 2885–2891.
- (33) Ma, Y.; Zhang, C.; Ji, G.; Lee, J. Y. Nitrogen-Doped Carbon-Encapsulation of Fe₃O₄ for Increased Reversibility in Li⁺ Storage by the Conversion Reaction. *J. Mater. Chem.* **2012**, *22*, 7845.
- (34) Piao, Y.; Kim, H. S.; Sung, Y. E.; Hyeon, T. Facile Scalable Synthesis of Magnetite Nanocrystals Embedded in Carbon Matrix as Superior Anode Materials for Lithium-Ion Batteries. *Chem. Commun. (Cambridge, U. K.)* **2010**, *46*, 118–20.
- (35) O'Neill, H. S.; Dollase, W. A. Crystal-Structures and Cation Distributions in Simple Spinel from Powder XRD Structural Refinements - MgCr₂O₄, ZnCr₂O₄, Fe₃O₄ and the Temperature-Dependence of the Cation Distribution in ZnAl₂O₄. *Phys. Chem. Miner.* **1994**, *20*, 541–555.
- (36) Badway, F.; Pereira, N.; Cosandey, F.; Amatucci, G. G. Carbon–Metal Fluoride Nanocomposites. *J. Electrochem. Soc.* **2003**, *150*, A1209.
- (37) Grosvenor, A. P.; Kobe, B. A.; Biesinger, M. C.; McIntyre, N. S. Investigation of Multiplet Splitting of Fe 2p XPS Spectra and Bonding in Iron Compounds. *Surf. Interface Anal.* **2004**, *36*, 1564–1574.
- (38) Van Vleck, J. H. The Dirac Vector Model in Complex Spectra. *Phys. Rev.* **1934**, *45*, 405–419.
- (39) Kozakov, A. T.; Kochur, A. G.; Googlev, K. A.; Nikolsky, A. V.; Raevski, I. P.; Smotrakov, V. G.; Yermkin, V. V. X-ray Photoelectron Study of the Valence State of Iron in Iron-containing Single-Crystal (BiFeO₃, PbFe_{1/2}Nb_{1/2}O₃), and Ceramic (BaFe_{1/2}Nb_{1/2}O₃) Multiferroics. *J. Electron Spectrosc.* **2011**, *184*, 16–23.
- (40) Chiuzaibaian, S. G.; Neumann, M.; Waldmann, O.; Schneider, B.; Bernt, I.; Saalfrank, R. W. X-ray Photoelectron Spectroscopy Study of a Cyclic Hexanuclear Cluster. *Surf. Sci.* **2001**, *482–485* (Part 2), 1272–1276.
- (41) McIntyre, N. S.; Zetaruk, D. G. X-ray Photoelectron Spectroscopic Studies of Iron Oxides. *Anal. Chem.* **1977**, *49*, 1521–1529.

- (42) Tiedtke, K.; Gerth, C.; Martins, M.; Zimmermann, P. Term-Dependent Lifetime Broadening in the 3p Photoelectron Spectra of Atomic Fe and Co. *Phys. Rev. A* **2001**, *64*, 022705.
- (43) Yamashita, T.; Hayes, P. Analysis of XPS Spectra of Fe²⁺ and Fe³⁺ Ions in Oxide Materials. *Appl. Sur. Sci.* **2008**, *254*, 2441–2449.
- (44) Thackeray, M. M.; David, W. I. F.; Goodenough, J. B. Structural Characterization of the Lithiated Iron Oxides Li_xFe₃O₄ and Li_xFe₂O₃. *Mater. Res. Bull.* **1982**, *17*, 785–793.
- (45) Thackeray, M. M.; Coetzer, J. A Preliminary Investigation of the Electrochemical Performance of α -Fe₂O₃ and Fe₃O₄ Cathodes in High-Temperature Cells. *Mater. Res. Bull.* **1981**, *16*, 591–597.
- (46) Fulvio, P. F.; Brown, S. S.; Adcock, J.; Mayes, R. T.; Guo, B.; Sun, X.-G.; Mahurin, S. M.; Veith, G. M.; Dai, S. Low-Temperature Fluorination of Soft-Templated Mesoporous Carbons for a High-Power Lithium/Carbon Fluoride Battery. *Chem. Mater.* **2011**, *23*, 4420–4427.
- (47) Toby, B. H.; EXPGUI, A. Graphical User Interface for GSAS. *J. Appl. Crystallogr.* **2001**, *34*, 210–213.
- (48) Krivanek, O. L.; Corbin, G. J.; Dellby, N.; Elston, B. F.; Keyse, R. J.; Murfitt, M. F.; Own, C. S.; Szilagyi, Z. S.; Woodruff, J. W. An Electron Microscope for the Aberration-Corrected Era. *Ultramicroscopy* **2008**, *108*, 179–195.